

Universal rules for the visible-light absorption in hybrid perovskite materials

Masato Kato¹, Takemasa Fujiseki¹, Tetsuhiko Miyadera², Takeshi Sugita²,
Shohei Fujimoto¹, Masato Tamakoshi¹, Masayuki Chikamatsu², and
Hiroyuki Fujiwara^{1*}

To realize ideal high-efficiency solar cells based on an organic-inorganic hybrid perovskite, a variety of perovskite compounds (APbX₃) consisting of mixed center cations (A = CH₃NH₃⁺, HC(NH₂)₂⁺, Cs⁺) with different PbX₃⁻ cages (X = I⁻, Br⁻, Cl⁻) have been fabricated. Nevertheless, there has been no clear understanding for the effects of A and X on the optical transitions. Here, we present universal rules that allow the interpretation and predication of the light absorption in the complex hybrid perovskite. In particular, our density functional theory analyses reveal that (i) the absorption strength in the visible region is governed by the strong interaction between A and X in the valence band and (ii) the effect of X on the absorption spectrum can be described simply by the general sum rule. Our calculations explain the drastic reduction of the absorption coefficient (α) in HC(NH₂)₂PbI₃ and confirm CsPbI₃ as the highest α material.

¹Department of Electrical, Electronic and Computer Engineering, Gifu University, 1-1 Yanagido, Gifu 501-1193, Japan. ²Research Center for Photovoltaics, National Institute of Advanced Industrial Science and Technology (AIST), Central 5, 1-1-1 Higashi, Tsukuba, Ibaraki 305-8568, Japan. *email: fujiwara@gifu-u.ac.jp

Numerous hybrid perovskite compounds expressed by APbX_3 (A: organic cation; X: halogen anion) have been investigated in an effort to develop high-efficiency hybrid perovskite solar cells¹⁻³⁵. Although extensive researches have been conducted on methylammonium lead iodide (MAPbI_3) perovskite¹⁻²⁰, now it becomes quite clear that MAPbI_3 exhibits large instability for temperature³⁻⁵, light illumination⁶, and humidity^{6,7}. In particular, MAPbI_3 shows the strong phase change at temperatures of ≥ 85 °C (refs. 4, 5), which is expected to limit the practical application of this material severely.

The thermal stability can be improved greatly when the A-site cation is replaced with formamidinium (FA)²¹. However, the FAPbI_3 perovskite is intrinsically unstable and cubic FAPbI_3 crystals ($\alpha\text{-FAPbI}_3$) show a gradual phase transformation into a transparent $\delta\text{-FAPbI}_3$ phase having a one-dimensional crystal structure^{22,23}. Quite fortunately, FAPbI_3 -based perovskites can be stabilized by including a small amount of MA^+ and Cs^+ having smaller ionic radii²⁴⁻³⁰. A recent study further demonstrates the improved overall stability of $\alpha\text{-FAPbI}_3$ by the incorporation of Cs and Br atoms³⁰. To date, very high conversion efficiencies exceeding 20% have been demonstrated in (FA, MA) $\text{Pb}(\text{I}, \text{Br})_3$ and (FA, MA, Cs) $\text{Pb}(\text{I}, \text{Br})_3$ solar cells^{25,30-32}.

Nevertheless, despite the rapid progress for the perovskite solar cell fabrication, the optical transitions in complex hybrid perovskites are not understood well. More specifically, the dielectric functions ($\varepsilon = \varepsilon_1 - i\varepsilon_2$) of $\alpha\text{-FAPbX}_3$ and CsPbX_3 have not been reported yet. Although many density functional theory (DFT) studies on FAPbI_3 (refs. 33, 34) and CsPbI_3 (refs. 15, 16, 36) have been conducted, the influence of the A-site cation and the X-site anion on the visible-light absorption has not been studied systematically.

In this work, we establish universal rules that allow the quantitative description of the optical absorption in various hybrid perovskites. Our DFT calculation reveals that the absorption coefficient (α) of the hybrid perovskites in the visible region is determined by the quite strong interaction of the X-site valence electron with the A-site cation, whereas the variation of the optical spectrum with the X-site anion can be expressed from the well-known sum rule³⁷. Based on the guiding principles established in this work, the α spectra of complex hybrid perovskites at room temperature can be predicated.

Optical constants of hybrid perovskite materials

Fig. 1 presents the α spectrum and dielectric function of an $\alpha\text{-FAPbI}_3$ layer fabricated in this work (Supplementary Fig. 1), together with those of MAPbI_3 (ref. 5), MAPbBr_3

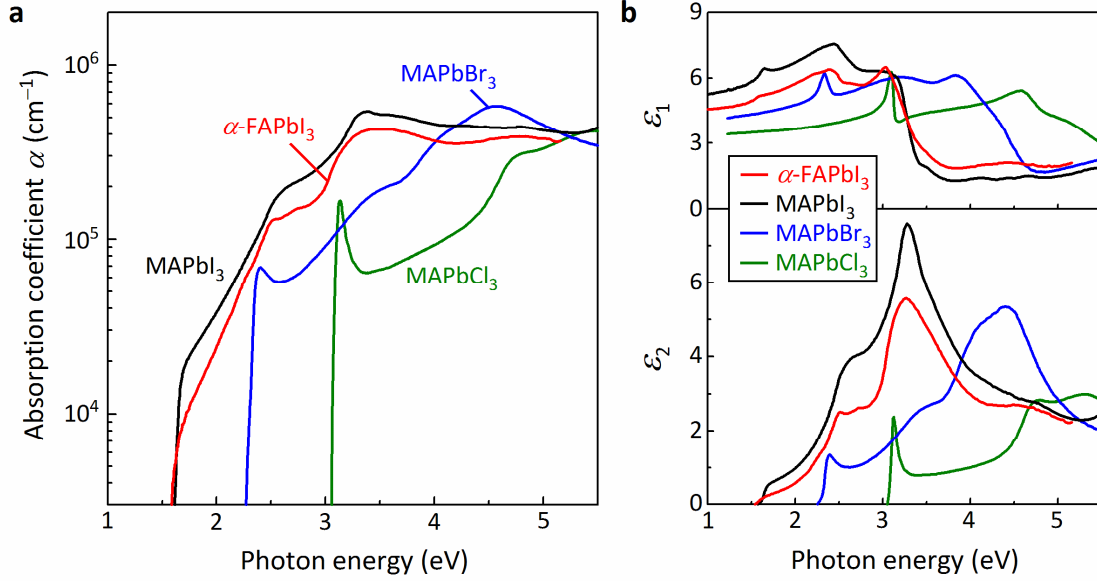


Figure 1 | Optical constants of α -FAPbI₃ and MAPbX₃. Optical data of α -FAPbI₃ determined in this work and reported optical data of MAPbI₃ (ref. 5), MAPbBr₃ (ref. 9), and MAPbCl₃ (ref. 9). **a**, α spectra of α -FAPbI₃ and MAPbX₃. **b**, Dielectric functions of α -FAPbI₃ and MAPbX₃.

(ref. 9) and MAPbCl₃ (ref. 9) reported earlier. We find that the α values of α -FAPbI₃ are much smaller than those of MAPbI₃ (Fig. 1a). This result is consistent with the experimental fact that thicker absorber layers (\sim 500 nm) are generally necessary for FAPbI₃-based perovskite solar cells^{25,30-32}, compared with MAPbI₃-based solar cells (typically \sim 300 nm)¹. The low α values in α -FAPbI₃ have also been justified from our external quantum efficiency (EQE) analysis performed for a reported high-efficiency FAPbI₃ solar cell²⁵ (see Method, Supplementary 2). Accordingly, the replacement of the center cation has a large impact on the absorption properties. The Urbach energy (E_U) of α -FAPbI₃ determined from Fig. 1a is 16 meV, supporting the suppressed tail state formation, as observed in MAPbI₃ ($E_U = 14$ – 15 meV)^{5,10} and (FA, Cs)Pb(I, Br)₃ ($E_U = 16$ meV)²⁹. We have further determined the E_g of α -FAPbI₃ (1.55 ± 0.01 eV) from the critical point (CP) analysis³⁸ using an established procedure⁵ (Supplementary Fig. 3). We also note that the dielectric function of δ -FAPbI₃ is quite different from that of α -FAPbI₃ (Supplementary Fig. 4).

For the change of the X anion in MAPbX₃, the whole dielectric function shifts toward higher energy and the amplitude of the ϵ_2 spectrum gradually reduces in the lighter halogen atom (Fig. 1b). The sharp absorption peaks observed near the E_g regions of

MAPbBr₃ and MAPbCl₃ are caused by the strong excitonic transitions³⁹. We further confirmed that the dielectric functions of FAPbI₃ and MAPbX₃ can be parameterized by assuming several Tauc-Lorentz transitions⁴⁰ (Supplementary Fig. 5 and Table I).

Optical transitions in α -FAPbI₃ and MAPbBr₃

To understand the optical transitions in the hybrid perovskites, we implemented the DFT calculations assuming pseudo-cubic structures, based on the generalized gradient approximation within the Perdew-Burke-Ernzerhof scheme (PBE)⁴¹ without considering spin-orbit coupling (SOC) (see Method). In Fig. 2a, α -FAPbI₃ and MAPbBr₃ crystal structures determined from the DFT are shown. The orientation of FA⁺ in Fig. 2a has been confirmed in a recent α -FAPbI₃ characterization using neutron powder diffraction²³.

In Fig. 2b, the experimental ε_2 spectrum of α -FAPbI₃ is compared with the ε_2 spectra that are calculated for the different polarization states with directions parallel to the a , b , and c axes in Fig. 2a. The DFT calculation reveals the highly anisotropic optical behavior of α -FAPbI₃ and the ε_2 spectra for the a and b axes (ε_a and ε_b) exhibit quite different shapes from that for the c axis (ε_c). Although the anisotropic optical properties of α -FAPbI₃ have not been reported in earlier studies^{33,34}, the α spectrum calculated from the ε_c in Fig. 2b shows quite good agreement with that calculated based on the GW method with SOC³³ (Supplementary Fig. 6). In Fig. 2b, the ε_c reproduces the fine absorption features observed experimentally at $E = 2\text{--}3$ eV and shows the remarkable overall agreement with the experimental result.

In Fig. 2c, the DFT results for MAPbBr₃ and MAPbI₃ are shown. The experimental and DFT data of MAPbI₃ are taken from our previous study⁵, in which the DFT calculation was performed in a similar way. For the MAPbBr₃, all the calculated spectra have been shifted toward higher energy by 0.22 eV to match the DFT result with the experimental result. The strong anisotropic behaviors are also confirmed in MAPbBr₃ and MAPbI₃, and the calculated ε_b and ε_c spectra reproduce the experimental results surprisingly well.

Our DFT calculations were performed without incorporating electron-hole interactions, and thus the excitonic transitions observed in MAPbBr₃ and MAPbCl₃ are not reproduced in the DFT results (see Supplementary Fig. 7 for MAPbCl₃). For the other transitions in α -FAPbI₃ and MAPbX₃, we find that the calculated ε_2 values are essentially larger than the experimental ε_2 values, indicating that the overall transitions are non-excitonic. In other words, the exciton formation is negligible in α -FAPbI₃.

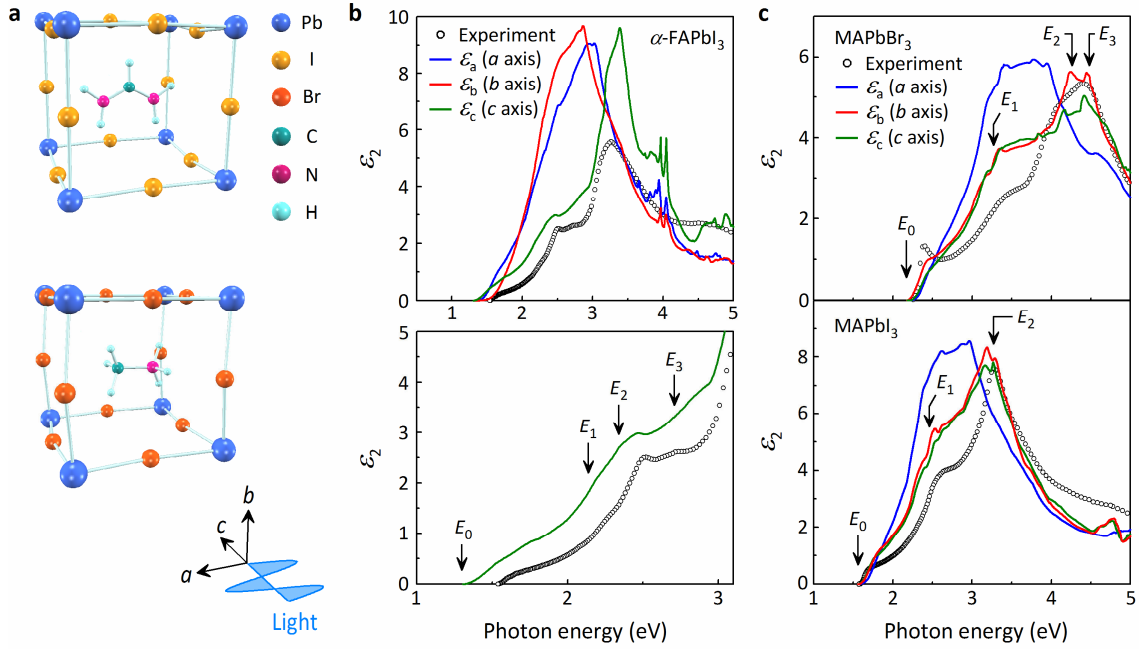


Figure 2 | ϵ_2 spectra of α -FAPbI₃, MAPbBr₃ and MAPbI₃ calculated by DFT. a, Pseudo-cubic crystal structures of α -FAPbI₃ and MAPbBr₃ obtained from the DFT calculations. Polarization states parallel to the a , b , and c axes are considered. **b**, ϵ_2 spectra of α -FAPbI₃, obtained from the experiment (open circles) and DFT calculations (solid lines). The experimental result corresponds to that shown in Fig. 1b. The ϵ_a , ϵ_b and ϵ_c represent the ϵ_2 spectra calculated assuming the light polarization along the a , b , and c axes in **a**, respectively. For the ϵ_c , the ϵ_2 spectra in two different energy regions are shown for clarity. The transition energies determined by the DFT analysis are indicated by arrows. **c**, ϵ_2 spectra of MAPbBr₃ and MAPbI₃, obtained from the experiment (open circles) and DFT calculations (solid lines). For the experimental data, the reported results of MAPbBr₃ (ref. 9) and MAPbI₃ (ref. 5) are shown. The DFT calculation result for MAPbBr₃ has been shifted toward higher energy by 0.22 eV to obtain better matching, whereas the DFT data of MAPbI₃ are taken from our earlier study⁵. The ϵ_a , ϵ_b and ϵ_c represent the ϵ_2 spectra calculated assuming the light polarization along the a , b , and c axes of the corresponding unit cell. The transition energies determined by the DFT analysis are indicated by arrows.

We further calculated the band structure and density of states (DOS) of α -FAPbI₃ (Fig. 3a) and MAPbBr₃ (Fig. 3b). For MAPbBr₃, however, the energy positions of all the conduction bands are shifted upward by 0.22 eV (scissors operation). Since the assumed pseudo-cubic structures are distorted, the energy positions of M_{1-3} and X_{1-3} differ slightly. The V_j and C_j denote the j th valence and conduction bands from the valence band maximum (VBM) and the conduction band minimum, respectively.

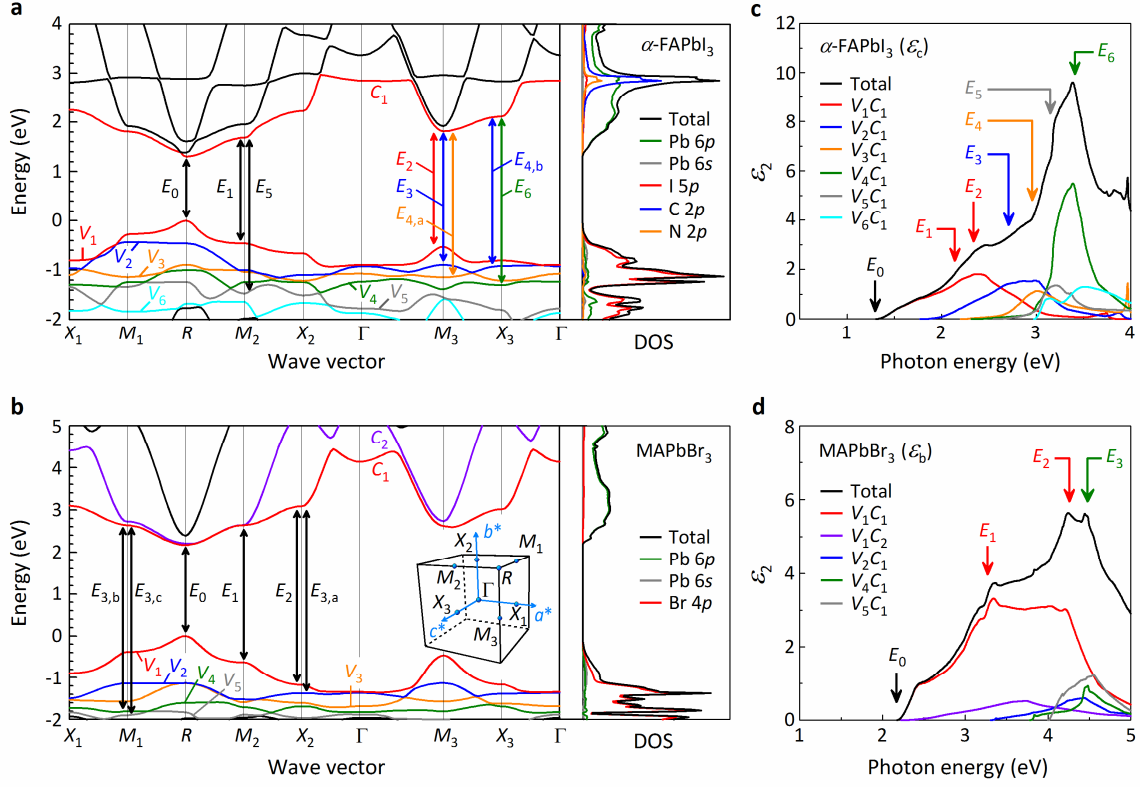


Figure 3 | Optical transition analyses for α -FAPbI₃ and MAPbBr₃ by DFT. **a**, Band structure and DOS of the pseudo-cubic α -FAPbI₃ crystal. The optical transitions determined by the polarization-dependent DFT analysis are indicated by arrows. The V_j and C_j denote the j th valence and conduction bands from the valence band maximum and the conduction band minimum, respectively. The transition energies of the $E_{4,a}$ at the M_3 point and $E_{4,b}$ at the X_3 point are almost identical. Partial DOS distributions are also indicated. **b**, Band structure and DOS of the pseudo-cubic MAPbBr₃ crystal. All the conduction bands have been shifted upward by 0.22 eV to improve the agreement with the experimental result. The optical transitions determined by the polarization-dependent DFT analysis are indicated by arrows. The transition energies of the $E_{3,a}$ (X_2 point), $E_{3,b}$ (M_1 point) and $E_{3,c}$ (M_1 point) are almost identical. The inset shows the high symmetry points in the Brillouin zone defined by the reciprocal lattices ($a^* = 2\pi/a$, $b^* = 2\pi/b$, $c^* = 2\pi/c$) for the assumed pseudo-cubic structure. Partial DOS distributions are also indicated. **c**, Contribution of various interband transitions to the ϵ_2 spectrum of α -FAPbI₃ calculated for the c -axis polarization (ϵ_c). V_jC_k denotes the interband transition from the j th valence band to the k th conduction band. Only the transitions with a peak amplitude of $\epsilon_2 > 1.0$ are shown for clarity and the ϵ_2 spectrum denoted as “Total” corresponds to the ϵ_c shown in Fig. 2b. The transition energies (E_{0-6}) determined from the DFT analysis are also indicated. **d**, Contribution of various interband transitions to the ϵ_2 spectrum of MAPbBr₃ calculated for the b -axis polarization (ϵ_b). Only the transitions with a peak amplitude of $\epsilon_2 > 0.5$ are shown for clarity. The transition energies (E_{0-3}) determined from the DFT analysis are also indicated.

V_1 mainly consists of the I $5p$ state in α -FAPbI₃ and the Br $4p$ state in MAPbBr₃, whereas C_1 is dominated by the Pb $6p$ in both α -FAPbI₃ and MAPbBr₃. For these perovskites, the optical transitions in the visible region occur predominantly from the X valence states to the Pb-derived conduction states, as confirmed for MAPbX₃ (ref. 8).

The contribution of each interband transition to the ε_2 spectrum is calculated further for the ε_c of α -FAPbI₃ (Fig. 3c) and the ε_b of MAPbBr₃ (Fig. 3d), and $V_j C_k$ denotes the transition from the j th valence band to the k th conduction band. Based on the procedure established previously⁵, we selected the optical transitions at high symmetry points that satisfy van Hove singularities³⁷, as indicated by the arrows in Fig. 3. In Fig. 2, the same transition energies have been indicated.

α -FAPbI₃ and MAPbBr₃ are direct transition semiconductors with the E_0 (E_g) transitions at the R point (cubic symmetry)^{9,34,35}. Our analyses further show that the interband transitions in α -FAPbI₃ are dominated by the transitions to C_1 , and C_j ($j \geq 2$) does not involve in the visible-light absorption. In α -FAPbI₃, the interband transition at low energies ($E < 3.2$ eV) is characterized by V_j ($j \leq 5$) \rightarrow C_1 transitions that occur predominantly at the M point (E_{1-5} transitions), whereas the intense ε_2 peak at 3.4 eV is attributed to the $V_4 C_1$ transition at the X_3 point (E_6 transition). In MAPbBr₃, the optical transition occurs mainly by the $V_1 C_1$ transition (Fig. 3d), and the E_1 , E_2 and E_3 peaks of the ε_b are attributed primarily to the transitions at the M_2 ($V_1 C_1$), X_2 ($V_1 C_1$) and M_1 ($V_4 C_1$) points, respectively. The overall ε_2 spectrum of MAPbI₃ is quite similar to that of MAPbBr₃, but MAPbI₃ shows a single transition peak in the high energy region (E_2 transition), as the transition energies of the X_2 ($V_1 C_1$) and M_1 ($V_4 C_1$) are almost the same in MAPbI₃ (ref. 5). For MAPbBr₃, the optical transition analysis has also been made based on the quasiparticle self-consistent GW approximation with SOC⁹, although the assignments are slightly different.

The E_g of α -FAPbI₃ obtained from the DFT calculation (1.30 eV in Fig. 3a) is slightly smaller than that of MAPbI₃ (1.56 eV)⁵. The E_g of APbI₃ is determined primarily by the I–Pb–I bond angle^{11,12} and, when the cation size is larger, the I–Pb–I bond angle becomes collinear ($\sim 180^\circ$) and the E_g reduces¹¹. This phenomenon has been explained by the anti-bonding character of the Pb–I bonds^{11,12}.

Effects of A and X on the light absorption

Quite strong anisotropy observed for α -FAPbI₃, MAPbBr₃ and MAPbI₃ in Fig. 2 can be understood from the strong interaction between the A-site cation and the surrounding X-site anions. Fig. 4a presents the charge density profiles of α -FAPbI₃ and MAPbI₃ in

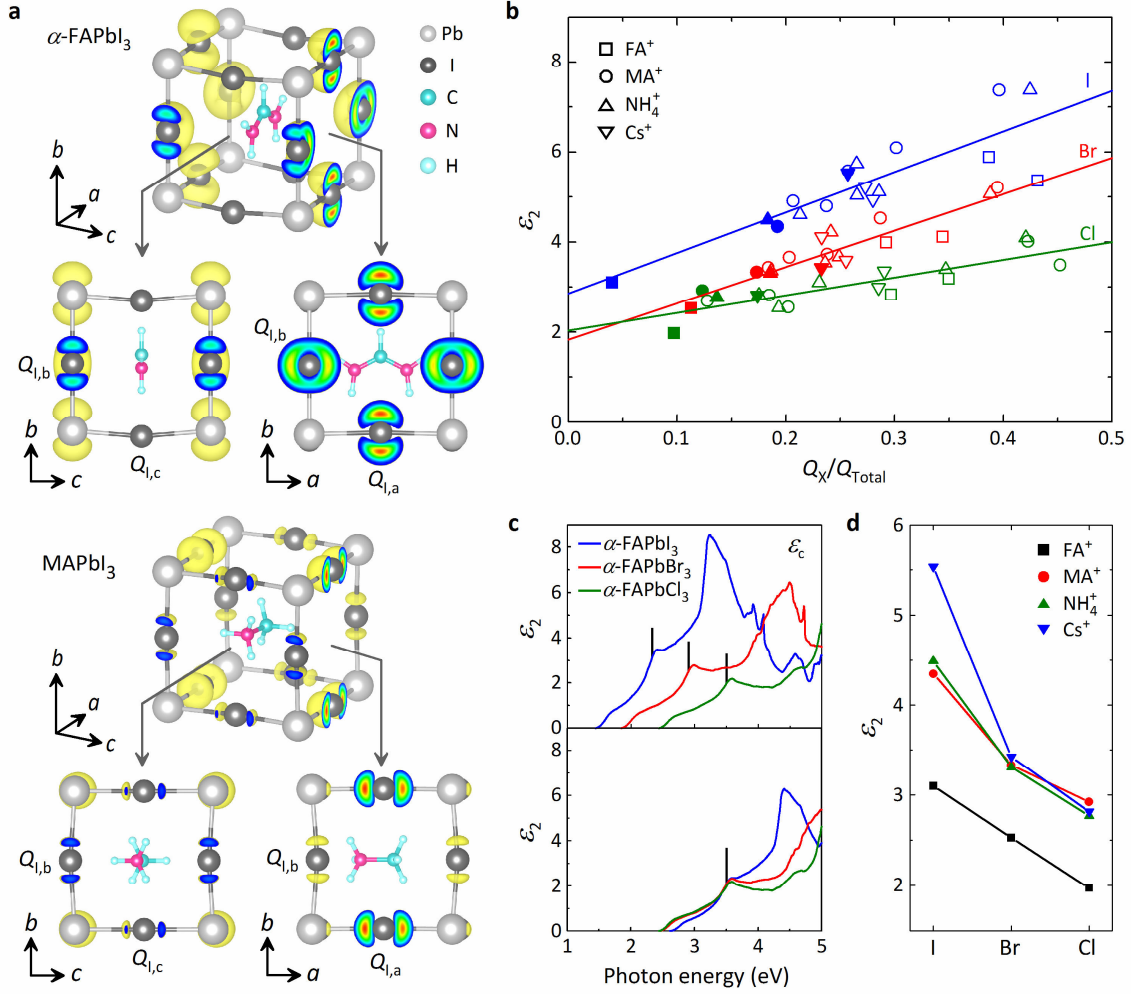


Figure 4 | Visible-light absorption determined by the valence charge density and the sum rule. **a**, Charge density profiles of α -FAPbI₃ and MAPbI₃ in the energy region of $-0.6 \sim -0.4$ eV from VBM ($E = 0$ eV). These profiles represent the valence charge densities for the E_2 transition (α -FAPbI₃) and the E_1 transition (MAPbI₃) at the M point. The charge densities of the I atoms along the a , b , and c axes are indicated as the $Q_{I,a}$, $Q_{I,b}$ and $Q_{I,c}$, respectively. **b**, ϵ_2 values for the optical transitions at the M_2 point (V_1C_1) in the APbX₃ ($A = \text{FA}^+$, MA^+ , NH_4^+ , Cs^+ ; $X = \text{I}^-$, Br^- , Cl^-) as a function of the charge density ratio (Q_X/Q_{Total}) in the corresponding valence-band energy region. The Q_X shows the valence charge density of the X-site atom along the a , b , and c axes that involves the optical absorption at the M point, and the Q_{Total} denotes the total charge density in the same energy region. The closed symbol represents the plot that shows the lowest Q_X/Q_{Total} among each APbX₃ material. **c**, Calculated ϵ_2 spectra of α -FAPbX₃ (top panel) and hypothetical ϵ_2 spectra of α -FAPbX₃ obtained by applying the sum rule after the energy-shift adjustment (bottom panel). The bars indicate the energy positions of the interband transition at the M_2 point (V_1C_1). **d**, ϵ_2 values of the closed symbols in **b**.

the energy region of $-0.6 \sim -0.4$ eV from VBM ($E = 0$ eV), which correspond to the valence charge densities for the E_2 transition (α -FAPbI₃) and E_1 transition (MAPbI₃) at the M point (V_1C_1). Here, we specifically consider the charge density distribution at the M point (V_1C_1), as the visible light absorption in the hybrid perovskites is determined essentially by the interband transitions near the M point (Fig. 3). The result for the MAPbI₃ was obtained from the optimized MAPbI₃ structure reported in our previous study⁵.

It can be seen from Fig. 4a that the charge density distributions of α -FAPbI₃ and MAPbI₃ are quite different. In particular, the valence electron of α -FAPbI₃ concentrates on the I atoms along the a and b axes, and the charge densities of these atoms ($Q_{1,a}$ and $Q_{1,b}$) are far larger than that of the c axis direction ($Q_{1,c}$). In contrast, the valence charge distribution is more uniform in MAPbI₃, although the $Q_{1,a}$ is larger than the $Q_{1,b}$ and $Q_{1,c}$. We find that the distribution of the $Q_{1,a-c}$ is determined by the strong interaction between the N and I. It is now established that, in MAPbI₃ (refs. 13, 14) and α -FAPbI₃ (ref. 23), the hydrogen bonding is formed between the N–H and I, which is expressed by $I(\delta^-)\cdots H(\delta^+)-N(\delta^-)$, where δ^+ and δ^- represent the positive and negative partial charges, respectively. Our systematic DFT calculations show that the interaction of the I and H–N further affects the $Q_{1,a-c}$ distribution, and the $Q_{1,a-c}$ reduces when the N–I distance is smaller (anti-coupling effect). In α -FAPbI₃, the valence electron concentrates on the a - b plane, whereas the $Q_{1,c}$ becomes quite small, due to the intense anti-coupling effect. In MAPbI₃, the larger $Q_{1,a}$, compared with the $Q_{1,b}$ and $Q_{1,c}$, can be interpreted by the strong N–I anti-coupling as the N atom locates close to the b - c plane.

The highly anisotropic optical transitions at the M point are governed almost completely by the anti-coupling effect. For the E_2 transition of α -FAPbI₃ (2.34 eV), for example, the ε_b shows the highest ε_2 value, while the ε_c indicates the lowest value (Fig. 2b). Since the $Q_{1,a}$ and $Q_{1,b}$ distributions of α -FAPbI₃ are oriented along the b axis (Fig. 4a), the polarizability increases significantly in this direction. Consequently, the ε_b of α -FAPbI₃ exhibits the maximum ε_2 value, while the quite small $Q_{1,c}$ leads to the drastic reduction of the transition probability and results in the decreased ε_c values. In the case of MAPbI₃, the $Q_{1,a}$ is aligned along the a axis, thus increasing the ε_a value at 2.5 eV (E_1 transition at the M_2 point⁵), whereas we observe $\varepsilon_b \sim \varepsilon_c$ since $Q_{1,b} \sim Q_{1,c}$. Moreover, when the N atom position of the MA⁺ is shifted toward the center position of the unit cell, the $Q_{1,a-c}$ distribution becomes uniform and the strong anisotropic properties disappear (Supplementary Fig. 8).

The above results indicate that the visible-light absorption is modified significantly by the anti-coupling effect. One important result in Fig. 2 is that, among the ε_2 spectra

calculated for different light polarizations, the ε_2 spectrum having the lowest values shows the best match with the experimental data. This result indicates the quite strong anti-coupling effect in the real material system. Although the cation position is fixed completely in the DFT, the cations in the actual perovskites reorient rapidly with a time scale of ~ 1 ps (refs. 13, 23, 42). Furthermore, the molecular dynamics simulation of MAPbI₃ confirms the strong interaction between the I and H–N, which maintains a stable I–H distance of 2.65 Å at 268 K (ref. 13). Thus, the anti-coupling phenomenon persists even at room temperature and controls the visible absorption.

To investigate the anti-coupling effect, we calculated the dielectric functions of various APbX₃ perovskites with different A-site cations (FA⁺, MA⁺, NH₄⁺, Cs⁺) and X-site anions (I⁻, Br⁻, Cl⁻). In the calculations, the dielectric functions of the APbX₃ were obtained by replacing the A-site cation using the identical PbI₃⁻, PbBr₃⁻ and PbCl₃⁻ structures to determine the effect of the A-site cation on the optical absorption. For the PbX₃⁻ structures, we employed the configurations that were determined from the structural optimization of MAPbX₃. The dielectric functions of the MAPbX₃, NH₄PbX₃ and CsPbX₃ obtained from this procedure are essentially similar (Supplementary Fig. 9) and, for these perovskites, the ε_2 values for the E_1 transition at the M_2 point (V_1C_1) were extracted. For α -FAPbX₃, we also obtained the ε_2 values for the E_1 transition at the M_2 point (V_1C_1), as the energies of the E_1 and E_2 transitions are similar when the PbX₃⁻ structure derived from MAPbX₃ is assumed. In Fig. 4b, these ε_2 values of the APbX₃ are summarized as a function of the charge density ratio (Q_X/Q_{Total}). The Q_X shows the corresponding valence charge density of the X atom along the a , b , and c axes at the M point ($Q_{1,a-c}$ in Fig 4a, for example), while the Q_{Total} denotes the total charge density in the same energy region. Thus, the Q_X/Q_{Total} represents the degree of charge density dispersion for the valence electron that involves the optical absorption at the M point. The DFT calculations in Fig. 4b were implemented using different locations of the A-site cation (see Method).

In Fig. 4b, the linear increase of the ε_2 value with the Q_X/Q_{Total} is evident and the variations of the ε_2 values are represented quite well by the linear fitting results obtained for each different X. This result shows the presence of a universal rule for the effect of the A-site cation on the ε_2 value. The closed symbol in Fig. 4b represents the ε_2 value that shows the lowest Q_X/Q_{Total} in each APbX₃ material. Since the experimental optical properties are reproduced when the strong anti-coupling effect is considered, the ε_2 values of the closed symbols approximate the light absorption strength in the actual hybrid perovskites. It is obvious that α -FAPbX₃ shows the lowest ε_2 , compared with the other APbX₃ perovskites. Because the FA cation has two N atoms, α -FAPbX₃ exhibits a

quite large anti-coupling effect, which in turn reduces the visible-light absorption significantly, as observed in Fig. 1. In contrast, Cs^+ is stabilized at the center position of the PbX_3^- cage with the weak anti-coupling effect. As a result, CsPbI_3 shows the highest ε_2 value among all the APbX_3 perovskites investigated here. This is consistent with the observed increase of α by the incorporation of Cs into $\alpha\text{-FAPbI}_3$ ²⁶.

We find that the effect of the X on the ε_2 spectrum can be expressed simply by the general sum rule [i.e., $\int E\varepsilon_2(E)dE = \text{const.}$]³⁷. Fig. 4c (top panel) shows the ε_2 spectra of $\alpha\text{-FAPbX}_3$ calculated in Fig. 4b (ε_c), which indicate the spectrum shift toward higher energy with decreasing halogen mass. This spectral change can be reproduced almost perfectly based on the sum rule (Fig. 4c, bottom panel). Specifically, the sum rule requires that the ε_2 peak amplitude reduces to $E/(E + \Delta E)$ when the ε_2 spectrum is shifted toward higher energy by ΔE . If the whole ε_2 spectra of $\alpha\text{-FAPbI}_3$ and $\alpha\text{-FAPbBr}_3$ are shifted so that the E_1 transition energies match that of $\alpha\text{-FAPbCl}_3$ and the amplitude of the shifted ε_2 spectra is reduced further by applying the sum rule, all the spectra overlap quite well in the energy region of $E < 3.5$ eV. Similar results have also been obtained for MAPbX_3 , CsPbX_3 and NH_4PbX_3 (Supplementary Fig. 9). Accordingly, the ε_2 amplitude variation induced by the X can simply be interpreted by the change in the transition energy. In Fig. 4d, the ε_2 values of the closed symbols in Fig. 4b are summarized. It can be seen that the ε_2 values reduce systematically with the order of $\text{I} > \text{Br} > \text{Cl}$, independent of the species of the A-site cation.

The above results indicate that the effects of the A-site cation and X-site anion can be described separately according to the valence charge interaction and the sum rule, respectively. In particular, our result provides the clear evidence that the center cation plays a crucial role in the optical transitions of complex hybrid perovskites. Consequently, in $\alpha\text{-FAPbI}_3$, the E_g decreases slightly due to the collinear I–Pb–I bond formation^{11,12}, but the α decreases notably by the strong anti-coupling effect. In contrast, the introduction of small Cs^+ increases the α because of the weak anti-coupling effect with a slight increase in E_g by the PbI_6 tilting¹¹. Our DFT results demonstrate that experimental dielectric functions of various organic-inorganic hybrid perovskites can be predicted from simple DFT calculations applying PBE.

Methods

DFT calculation. The DFT calculations of various APbX_3 perovskite materials were implemented using a plane-wave ultrasoft pseudopotential method within PBE⁴¹ (Advance/PHASE software). We performed the structural optimization of α -FAPbI₃ and MAPbBr₃ structures using a $6 \times 6 \times 6$ k mesh and a plane-wave cutoff energy of 500 eV until the atomic configuration converged to within $10 \text{ meV } \text{\AA}^{-1}$. From these calculations, we obtained the lattice parameters of $a = 6.416 \text{ \AA}$, $b = 6.236 \text{ \AA}$, and $c = 6.353 \text{ \AA}$ with $\alpha = \beta = \gamma = 90.00^\circ$ (α -FAPbI₃) and $a = 5.934 \text{ \AA}$, $b = 5.919 \text{ \AA}$, and $c = 5.936 \text{ \AA}$ with $\alpha = \gamma = 90.00^\circ$ and $\beta = 89.94^\circ$ (MAPbBr₃). These lattice parameters show good agreement with the experimental results reported for α -FAPbI₃ (ref. 23) and MAPbBr₃ (ref. 7). The dielectric functions are calculated based on a method developed by Kageshima et al.⁴³. For this calculation, we use a more dense $10 \times 10 \times 10$ k mesh to suppress distortion of calculated spectra.

Previously, the importance of SOC in the DFT calculation of MAPbI₃ has been pointed out¹⁵⁻¹⁷ and the experimental E_g values of MAPbI₃ and α -FAPbI₃ are reproduced well when the effect of SOC is considered using the GW approximation^{17,18,33} or a hybrid functional¹⁹. However, the band structures obtained from these sophisticated calculations are essentially similar to that deduced from the simple PBE calculation^{5,20}. Thus, in this study, the PBE calculation is performed without incorporating the SOC effect.

In the DFT calculations of Fig. 4b, we implemented the structural optimization of the A-site cation ($\text{A} = \text{FA}^+$, MA^+ , NH_4^+ and Cs^+) within each PbX_3^- ($\text{X} = \Gamma, \text{Br}^-, \text{Cl}^-$) cage. However, the structural optimization of FA^+ was rather difficult when the PbX_3^- structures determined from MAPbX₃ were employed. For the orientation of FA^+ in α -FAPbX₃, therefore, we assumed a configuration similar to Fig. 2a. For MAPbX₃, we also performed the calculation by varying the N atom position within the PbX_3^- . Specifically, in this calculation, the N atom of MA^+ is shifted to the center position of the C-N bond in the optimized MAPbX₃ structure (see also Supplementary Fig. 8b). The location of the N atom in the optimized NH_4PbX_3 structure is quite similar to that of MA^+ in the corresponding MAPbX₃ structure (ref. 5). Accordingly, we also calculated the dielectric function of NH_4PbX_3 when NH_4^+ is placed at the center position of the unit cell. In the optimized CsPbX_3 , Cs^+ locates near the center position of the unit cell, and the dielectric functions were calculated only for the optimized structures of CsPbX_3 . On the other hand, for the calculation of the Q_X/Q_{Total} in Fig. 4b, we selected energy regions that correspond to the E_1 transitions at the M_2 point. In the actual Q_X/Q_{Total}

analyses, we employed the energy ranges of $-0.6 \sim -0.4$ eV (APbI₃), $-0.7 \sim -0.5$ eV (APbBr₃) and $-0.8 \sim -0.6$ eV (APbCl₃) from VBM ($E = 0$ eV).

FAPbI₃ preparation. α -FAPbI₃ and δ -FAPbI₃ layers were fabricated by a laser evaporation technique⁵, in which PbI₂ and FAI source materials are heated by a near-infrared laser with a wavelength of 808 nm (Pascal, PA-LH-30LD). This method allows the preparation of smooth perovskite layers, which is quite important for reliable optical analyses. We find that α -FAPbI₃ and δ -FAPbI₃ layers can be formed separately by choosing proper substrates. For the preparation of α -FAPbI₃, we employed crystalline Si (*c*-Si) substrates covered with native oxide, whereas δ -FAPbI₃ can be formed by using substrates in which thin PCDTBT (poly[N-9''-hepta-decanyl-2,7-carbazole-alt-5,5-(4',7'-di-2-thienyl-2',1',3'-benzothiadiazole)]) layers (~ 5 nm) are formed on ZnO-coated *c*-Si substrates. For the deposition of α -FAPbI₃, we particularly used uncleaned SiO₂/*c*-Si substrates, as ultrasonic cleaning of the substrates using organic solvents tends to increase the PbI₂ formation. In the laser evaporation process, the evaporation rates of the source materials were controlled by adjusting the laser power. The resulting α -FAPbI₃-layer deposition rate was 2.3 nm min⁻¹. The laser evaporation process was conducted without substrate heating at a pressure of 4×10^{-4} Pa.

The x-ray diffraction measurements of the α -FAPbI₃ samples confirm (100) and (200) diffraction peaks attributed to the cubic phase²³ without the presence of other diffraction peaks originating from δ -FAPbI₃ and PbI₂ secondary phases (Supplementary Fig. 1). For the α -FAPbI₃, however, the preparation of the smooth surface is more difficult compared with MAPbI₃, and the root-mean-square roughness (d_{rms}) of a 100-nm-thick FAPbI₃ layer is 10.9 nm (Supplementary Fig. 1), which is larger than the d_{rms} of 4.6 nm observed for a laser-evaporated MAPbI₃ layer⁵.

Dielectric function analysis. The dielectric functions of α -FAPbI₃ and δ -FAPbI₃ were determined by spectroscopic ellipsometry (SE). The SE measurements of FAPbI₃ layers were performed in a N₂ ambient without exposing the samples to air, as α -FAPbI₃ exhibits significant degradation in humid air^{3,21,26-28}. To avoid exposure of the samples to humid air, the samples are sealed in a plastic bag inside a N₂-filled glove box attached to the laser evaporation system. The plastic bag with the samples is then transferred to a glove bag, in which the ellipsometry instrument is placed, and the plastic bag is opened after the glove bag is filled with N₂. The actual SE measurements were implemented at an angle of incidence of 75° using a rotating-compensator ellipsometer³⁸ (J.A. Woollam M-2000XI).

The SE analyses of the α -FAPbI₃ layers were performed by using a global error minimization scheme⁴⁴, in which the dielectric function is determined self-consistently using more than two samples with different layer thicknesses. For the α -FAPbI₃ analysis, two samples with thicknesses of 100 and 200 nm in Supplementary Fig. 1 were used. From these samples with different α -FAPbI₃ layer thicknesses, two sets of ellipsometry spectra [i.e., $(\psi, \Delta)_{100\text{nm}}$ and $(\psi, \Delta)_{200\text{nm}}$] were obtained. In the first step of the self-consistent analysis, the dielectric function of the bulk layer $\varepsilon_{\text{bulk}}(E)$ is extracted directly from the $(\psi, \Delta)_{100\text{nm}}$ using a mathematical inversion³⁸ without assuming dielectric function models. For the mathematical inversion, we employed an optical model consisting of a surface roughness layer/ α -FAPbI₃ bulk layer/SiO₂ (2 nm)/*c*-Si substrate structure. The optical properties of the surface roughness layer were calculated as a 50:50 vol.% mixture of the bulk layer and voids by applying the Bruggeman effective-medium approximation (EMA)³⁸.

In the second step, the deduced $\varepsilon_{\text{bulk}}(E)$ is applied to the fitting analysis of the $(\psi, \Delta)_{200\text{nm}}$. For the optical model of this fitting analysis, we assumed a slight void component at the α -FAPbI₃/substrate interface and employed an optical model of surface roughness layer/ α -FAPbI₃ bulk layer/interface layer/SiO₂ (2 nm)/*c*-Si substrate. The optical properties of the interface layer were deduced from EMA assuming a mixture of α -FAPbI₃ and voids. In the SE analysis of the $(\psi, \Delta)_{200\text{nm}}$, the void volume fractions in the surface roughness and interface layers were varied as free parameters.

From the above multi-sample analysis procedure, $\varepsilon_{\text{bulk}}(E)$, the surface roughness layer thickness (d_s), the bulk layer thickness (d_b) and the interface layer thickness (d_{inter}) of the deposited layers can be determined, based on the assumption that the bulk-layer optical properties are independent of the layer thickness. In Supplementary Fig. 10, the fitting result of the $(\psi, \Delta)_{200\text{nm}}$ using the $\varepsilon_{\text{bulk}}(E)$ extracted from the $(\psi, \Delta)_{100\text{nm}}$ is shown. Unfortunately, the fitting quality degrades at $E \geq 3.0$ eV, which can be attributed to the effect of the rough surface observed in the α -FAPbI₃ (Supplementary Fig. 1). Thus, in the global-error-minimization analysis, the fitting error in the energy region of $E \leq 3.0$ eV was used, and we obtained $d_s = 1.7 \pm 0.1$ nm and $d_b = 92.1 \pm 0.1$ nm for the $(\psi, \Delta)_{100\text{nm}}$, whereas the values of $d_s = 19.3 \pm 0.6$ nm (void fraction: 32 ± 1 vol.%), $d_b = 153.5 \pm 1.1$ nm and $d_{\text{inter}} = 61.8 \pm 1.2$ nm (void fraction: 31 ± 1 vol.%) were obtained for the $(\psi, \Delta)_{200\text{nm}}$. In the subsequent analysis, we extracted the final α -FAPbI₃ dielectric function shown in Fig. 1b from the $(\psi, \Delta)_{100\text{nm}}$ by adjusting d_b slightly so that the ε_2 values become zero at $E < E_g$. This procedure was necessary as the ε_2 values determined in the above analysis show very small negative values at $E < E_g$. This d_b adjustment is minor and was made to within 2% of the total d_b . The d_s of 1.7 ± 0.1 nm obtained from

the above analysis is smaller than the value of $d_{\text{rms}} = 10.9$ nm obtained from the atomic force microscopy (AFM) image (Supplementary Fig. 1). Thus, the amplitude of the dielectric function in the high energy region ($E > 3$ eV), which was not used in the self-consistent SE analysis, could be underestimated by the effect of the rough surface.

A similar ellipsometry analysis was performed for δ -FAPbI₃ using two samples with thicknesses of 30 nm and 80 nm (Supplementary Fig. 1). For the mathematical inversion of the $(\psi, \Delta)_{30\text{nm}}$ obtained for the δ -FAPbI₃, we employed an optical model of surface roughness layer/ δ -FAPbI₃ bulk layer/PCDTBT layer (5 nm)/ZnO (50 nm)/*c*-Si substrate. From this SE analysis, the structure of the 30-nm-thick layer is determined to be $d_s = 7.9 \pm 0.1$ nm and $d_b = 29.6 \pm 0.1$ nm. The d_s of the δ -FAPbI₃ layer shows good agreement with the value of $d_{\text{rms}} = 5.7$ nm observed by AFM (Supplementary Fig. 1).

EQE analysis

Using the α -FAPbI₃ dielectric function in Fig. 1b, we analyzed the EQE spectrum of a reported FAPbI₃ solar cell consisting of a glass/SnO₂:F/compact TiO₂/mesoporous TiO₂- α -FAPbI₃/ α -FAPbI₃/polytriarylamine (PTAA)/Au structure²⁵. For the optical constants of the component layers, we employed reported data^{5,45}, although the optical constants of spiro-OMeTAD [2,2',7,7'-tetrakis-(N,N-di-p-methoxyphenylamine) 9,9'-spirobifluorene]⁵ were used for the PTAA layer, as the optical constants of PTAA have not been reported and the absorption properties of PTAA (ref. 46) are similar to those of spiro-OMeTAD. The optical response within the mesoporous TiO₂- α -FAPbI₃ mixed-phase layer was expressed by the two separate flat layers of the TiO₂ and α -FAPbI₃ assuming a porosity of 60% for the TiO₂ layer⁵. From this assumption, we constructed an optical model of glass/SnO₂:F (600 nm)/TiO₂ (120 nm)/ α -FAPbI₃ (590 nm)/spiro-OMeTAD (50 nm)/Au for the solar cell. The actual EQE calculation was implemented based on the optical admittance method in which the absorptance of each component layer is deduced by assuming a flat layer structure^{47,48}. However, since the reflectance (*R*) spectrum of the perovskite solar cell has not been reported, we performed the EQE calculation assuming a fixed *R* value of 10% in the calculation procedure of ref. 48. The *R* value of $\sim 10\%$ has been observed in MAPbI₃ solar cells having similar structures². The EQE spectrum of the solar cell was determined assuming 100% collection of photocarriers generated within the α -FAPbI₃ absorber layer (Supplementary Fig. 2).

References

1. Liu, M., Johnston, M. B. & Snaith, H. J. Efficient planar heterojunction perovskite solar cells by vapour deposition. *Nature* **501**, 395–398 (2013).
2. Heo, J. H. *et al.* Efficient inorganic-organic hybrid heterojunction solar cells containing perovskite compound and polymeric hole conductors. *Nature Photon.* **7**, 486–492 (2013).
3. Stoumpos, C. C., Malliakas, C. D. & Kanatzidis, M. G. Semiconducting tin and lead iodide perovskites with organic cations: phase transitions, high mobilities, and near-infrared photoluminescent properties. *Inorg. Chem.* **52**, 9019–9038 (2013).
4. Conings, B. *et al.* Intrinsic thermal instability of methylammonium lead trihalide perovskite. *Adv. Energy Mater.* **5**, 1500477 (2015).
5. Shirayama, M. *et al.* Optical transitions in hybrid perovskite solar cells: Ellipsometry, density functional theory, and quantum efficiency analyses for CH₃NH₃PbI₃. *Phys. Rev. Applied* **5**, 014012 (2016).
6. Niu, G., Guo, X. & Wang, L. Review of recent progress in chemical stability of perovskite solar cells. *J. Mater. Chem. A* **3**, 8970–8980 (2015).
7. Noh, J. H., Im, S. H., Heo, J. H., Mandal, T. N. & Seok, S. I. Chemical management for colorful, efficient, and stable inorganic-organic hybrid nanostructured solar cells. *Nano Lett.* **13**, 1764–1769 (2013).
8. Mosconi, E., Amat, A., Nazeeruddin, M. K., Grätzel, M. & De Angelis, F. First-principles modeling of mixed halide organometal perovskites for photovoltaic applications. *J. Phys. Chem. C* **117**, 13902–13913 (2013).
9. Leguy, A. M. A. *et al.* Experimental and theoretical optical properties of methylammonium lead halide perovskites. *Nanoscale* **8**, 6317–6327 (2016).
10. De Wolf, S. *et al.* Organometallic halide perovskites: Sharp optical absorption edge and relation to photovoltaic performance. *J. Phys. Chem. Lett.* **5**, 1035–1039 (2014).
11. Filip, M. R., Eperon, G. E., Snaith, H. J. & Giustino, F. Steric engineering of metal-halide perovskites with tunable optical band gaps. *Nature Commun.* **5**, 5757 (2014).
12. Kim, J., Lee, S.-C., Lee, S.-H. & Hong, K.-H. Importance of orbital interactions in determining electronic band structures of organo-lead iodide. *J. Phys. Chem. C* **119**, 4627–4634 (2015).
13. Mosconi, E., Quarti, C., Ivanovska, T., Ruani, G. & De Angelis, F. Structural and electronic properties of organo-halide lead perovskites: A combined IR-spectroscopy and *ab initio* molecular dynamics investigation. *Phys. Chem. Chem.*

- Phys.* **16**, 16137–16144 (2014).
14. Lee, J.-H., Bristowe, N. C., Bristowe, P. D. & Cheetham, A. K. Role of hydrogen-bonding and its interplay with octahedral tilting in CH₃NH₃PbI₃. *Chem. Commun.* **51**, 6434–6437 (2015).
 15. Even, J., Pedesseau, L., Jancu, J.-M. & Katan, C. Importance of spin-orbit coupling in hybrid organic/inorganic perovskites for photovoltaic applications. *J. Phys. Chem. Lett.* **4**, 2999–3005 (2013).
 16. Even, J., Pedesseau, L., Jancu, J.-M. & Katan, C. DFT and *k*-*p* modelling of the phase transitions of lead and tin halide perovskites for photovoltaic cells. *Phys. Status Solidi RRL* **8**, 31–35 (2014).
 17. Umari, P., Mosconi, E. & De Angelis, F. Relativistic GW calculations on CH₃NH₃PbI₃ and CH₃NH₃SnI₃ perovskites for solar cell applications. *Sci. Rep.* **4**, 4467 (2014).
 18. Brivio, F., Butler, K. T. & Walsh, A. Relativistic quasiparticle self-consistent electronic structure of hybrid halide perovskite photovoltaic absorbers. *Phys. Rev. B* **89**, 155204 (2014).
 19. Menéndez-Proupin, E., Palacios, P., Wahnón, P. & Conesa, J. C. Self-consistent relativistic band structure of the CH₃NH₃PbI₃ perovskite. *Phys. Rev. B* **90**, 045207 (2014).
 20. Yin, W.-J., Yang, J.-H., Kang, J., Yan, Y. & Wei, S.-H. Halide perovskite materials for solar cells: A theoretical review. *J. Mater. Chem. A* **3**, 8926–8942 (2015).
 21. Eperon, G. E. *et al.* Formamidinium lead trihalide: A broadly tunable perovskite for efficient planar heterojunction solar cells. *Energy Environ. Sci.* **7**, 982–988 (2014).
 22. Han, Q. *et al.* Single crystal formamidinium lead iodide (FAPbI₃): Insight into the structural, optical, and electrical properties. *Adv. Mater.* **28**, 2253–2258 (2016).
 23. Weller, M. T., Weber, O. J., Frost, J. M. & Walsh, A. Cubic perovskite structure of black formamidinium lead iodide, α -[HC(NH₂)₂]PbI₃, at 298 K. *J. Phys. Chem. Lett.* **6**, 3209–3212 (2015).
 24. Pellet, N. *et al.* Mixed-organic-cation perovskite photovoltaics for enhanced solar-light harvesting. *Angew. Chem. Int. Ed.* **53**, 3151–3157 (2014).
 25. Yang, W. S. *et al.* High-performance photovoltaic perovskite layers fabricated through intramolecular exchange. *Science* **348**, 1234–1237 (2015).
 26. Lee, J.-W. *et al.* Formamidinium and cesium hybridization for photo- and moisture-stable perovskite solar cell. *Adv. Energy Mater.* **5**, 1501310 (2015).
 27. Li, Z. *et al.* Stabilizing perovskite structures by tuning tolerance factor: Formation of formamidinium and cesium lead iodide solid state. *Chem. Mater.* **28**, 284–292

- (2016).
28. Yi, C. *et al.* Entropic stabilization of mixed A-cation ABX₃ metal halide perovskites for high performance perovskite solar cells. *Energy Environ. Sci.* **9**, 656–662 (2016).
 29. McMeekin, D. P. *et al.* A mixed-cation lead mixed-halide perovskite absorber for tandem solar cells. *Science* **351**, 151–155 (2016).
 30. Saliba, M. *et al.* Cesium-containing triple cation perovskite solar cells: Improved stability, reproducibility and high efficiency. *Energy Environ. Sci.* doi: 10.1039/c5ee03874j (2016).
 31. Bi, D. *et al.* Efficient luminescent solar cells based on tailored mixed-cation perovskites. *Sci. Adv.* **2**, e1501170 (2016).
 32. Jacobsson, T. J. *et al.* Exploration of the compositional space for mixed lead halogen perovskites for high efficiency solar cells. *Energy Environ. Sci.* doi: 10.1039/c6ee00030d (2016).
 33. Amat, A. *et al.* Cation-induced band-gap tuning in organohalide perovskites: interplay of spin-orbit coupling and octahedral tilting. *Nano Lett.* **14**, 3608–3616 (2014).
 34. Li, D., Meng, J., Niu, Y., Zhao, H. & Liang, C. Understanding the low-loss mechanism of general organic-inorganic perovskites from first-principles calculation. *Chem. Phys. Lett.* **627**, 13–19 (2015).
 35. Park, J.-S. *et al.* Electronic structure and optical properties of α -CH₃NH₃PbBr₃ perovskite single crystal. *J. Phys. Chem. Lett.* **6**, 4304–4308 (2015).
 36. Brgoch, J., Lehner, A. J., Chabinyk, M. & Seshadri, R. Ab initio calculations of band gaps and absolute band positions of polymorphs of RbPbI₃ and CsPbI₃: Implications for main-group halide perovskite photovoltaics. *J. Phys. Chem. C* **118**, 27721–27727 (2014).
 37. Marder, M. P. *Condensed Matter Physics* (Wiley, Hoboken, 2010).
 38. Fujiwara, H. *Spectroscopic Ellipsometry: Principles and Applications* (Wiley, West Sussex, 2007).
 39. Kitazawa, N., Watanabe, Y. & Nakamura, Y. Optical properties of CH₃NH₃PbX₃ (X = halogen) and their mixed-halide crystals. *J. Mater. Sci.* **37**, 3585–3587 (2002).
 40. Jellison, Jr., G. E. & Modine, F. A. Parameterization of the optical functions of amorphous materials in the interband region. *Appl. Phys. Lett.* **69**, 371–373 (1996); Erratum, *Appl. Phys. Lett.* **69**, 2137 (1996).
 41. Perdew, J. P., Burke, K. & Ernzerhof, M. Generalized gradient approximation made simple. *Phys. Rev. Lett.* **77**, 3865–3868 (1996).

42. Wasylishen, R. E., Knop, O. & Macdonald, J. B. Cation rotation in methylammonium lead halides. *Solid State Commun.* **56**, 581–582 (1985).
43. Kageshima, H. & Shiraishi, K. Momentum-matrix-element calculation using pseudopotentials. *Phys. Rev. B* **56**, 14985–14992 (1997).
44. Fujiwara, H., Koh, J., Rovira, P. I. & Collins, R. W. Assessment of effective-medium theories in the analysis of nucleation and microscopic surface roughness evolution for semiconductor thin films. *Phys. Rev. B* **61**, 10832–10844 (2000).
45. Adachi, S. *The Handbook on Optical Constants of Metals: In Tables and Figures* (World Scientific, Singapore, 2012).
46. Kwon, J.-H. *et al.* Channel width effect for organic thin film transistors using TIPS-pentacene employed as a dopant of poly-triarylamine. *Organic Electronics* **10**, 729–734 (2009).
47. Macleod, H. A. *Thin-Film Optical Filters* (CRC Press, NY, 2010).
48. Hara, T. *et al.* Quantitative assessment of optical gain and loss in submicron-textured $\text{CuIn}_{1-x}\text{Ga}_x\text{Se}_2$ solar cells fabricated by three-stage coevaporation. *Phys. Rev. Applied* **2**, 034012 (2014).

Author contributions

M.K. carried out the DFT calculations and T.F. performed the perovskite characterization. T.M. designed the laser evaporation process with the help of M.C., and T.S. fabricated the perovskite layers. S.F. contributed to the optical function analysis and M.T. performed the EQE simulation. H.F. directed the study and prepared the manuscript.

Competing financial interests

The authors declare no competing financial interests.

Supplementary Information

Universal rules for the visible-light absorption in hybrid perovskite materials

Masato Kato¹, Takemasa Fujiseki¹, Tetsuhiko Miyadera², Takeshi Sugita²,
Shohei Fujimoto¹, Masato Tamakoshi¹, Masayuki Chikamatsu², and
Hiroyuki Fujiwara^{1*}

¹Department of Electrical, Electronic and Computer Engineering, Gifu University, 1-1 Yanagido, Gifu 501-1193, Japan. ²Research Center for Photovoltaics, National Institute of Advanced Industrial Science and Technology (AIST), Central 5, 1-1-1 Higashi, Tsukuba, Ibaraki 305-8568, Japan.

*E-mail: fujiwara@gifu-u.ac.jp

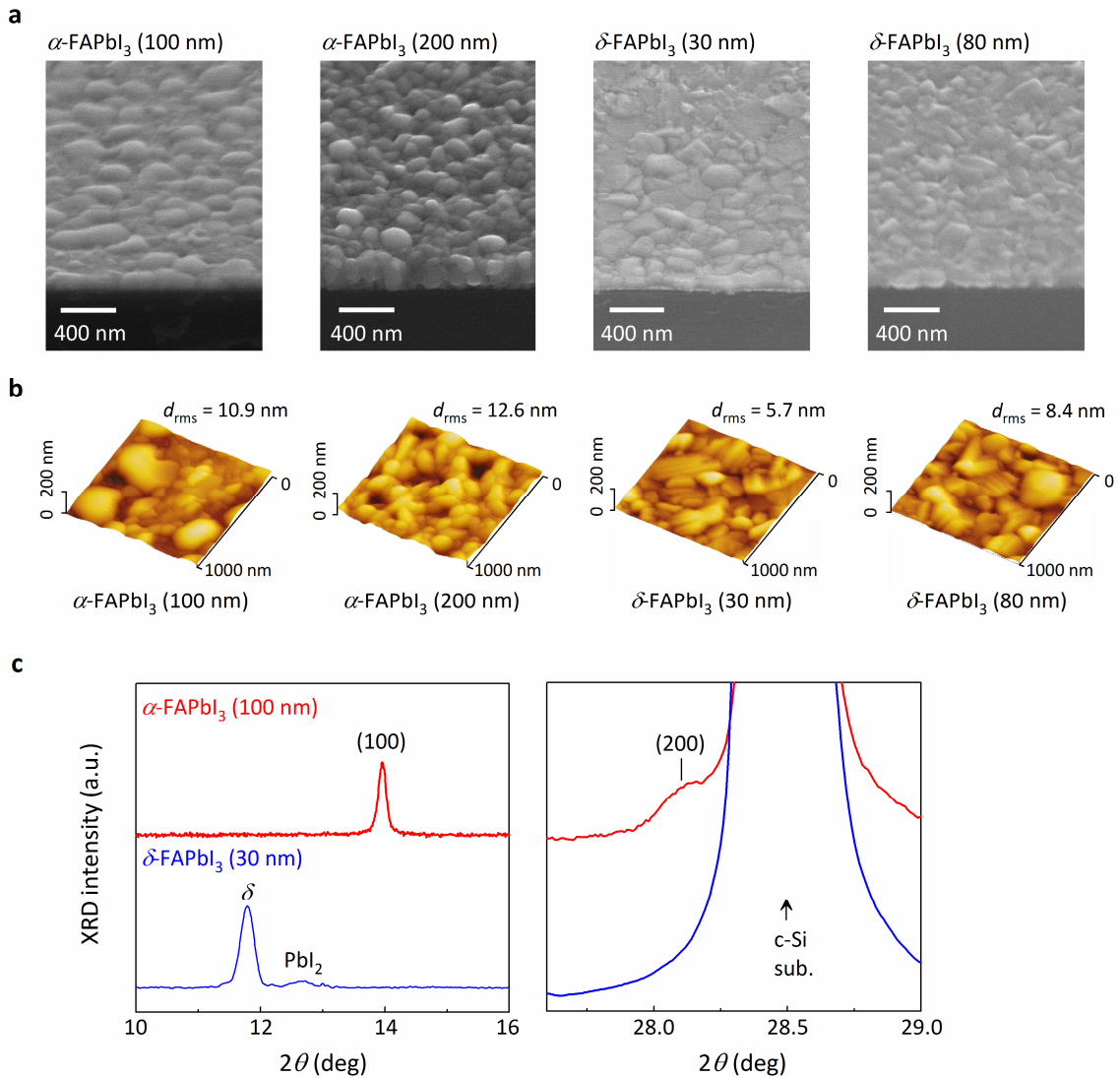


Figure S1 | Surface and crystal structures of FAPbI₃ layers. **a**, Scanning electron microscope images of the α -FAPbI₃ and δ -FAPbI₃ layers fabricated by laser evaporation processes. The α -FAPbI₃ and δ -FAPbI₃ layers were prepared separately by using SiO₂(2 nm)/c-Si and PCDTBT(5 nm)/ZnO (50 nm)/c-Si substrates, respectively. **b**, AFM images of the α -FAPbI₃ and δ -FAPbI₃ layers. The d_{rms} values obtained from the AFM images are also indicated. **c**, XRD spectra of the α -FAPbI₃ (100 nm) and δ -FAPbI₃ (30 nm) in **a**.

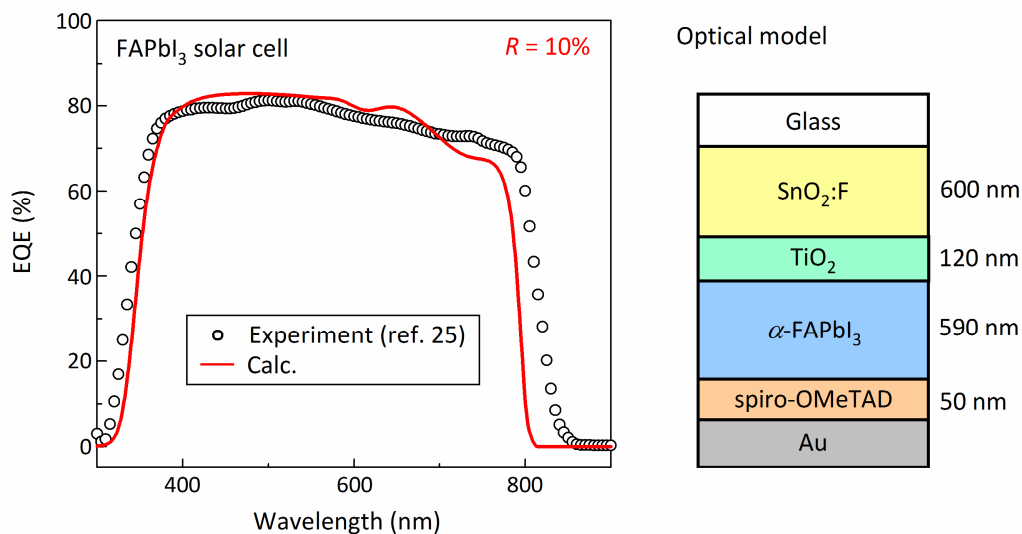


Figure S2 | EQE analysis for a FAPbI₃ hybrid perovskite solar cell. EQE spectrum of a FAPbI₃ hybrid perovskite solar cell having a structure of glass/SnO₂:F/compact TiO₂/mesoporous TiO₂-α-FAPbI₃/uniform α-FAPbI₃/polytriarylamine (PTAA)/Au structure was analyzed. The open circles show the experimental data reported in ref. 25, whereas the solid line represents the EQE spectrum calculated using an optical model consisting of glass/SnO₂:F (600 nm)/TiO₂ (120 nm)/α-FAPbI₃ (590 nm)/spiro-OMeTAD (50 nm)/Au structure. In the EQE calculation, the *R* of the solar cell is assumed to be 10% in the whole wavelength region. The absorption onset of the α-FAPbI₃ observed in the experimental EQE spectrum is ~840 nm and shows a slight red shift, compared with the EQE calculation result (~800 nm). This effect could be attributed to the tail absorption in the solar cell.

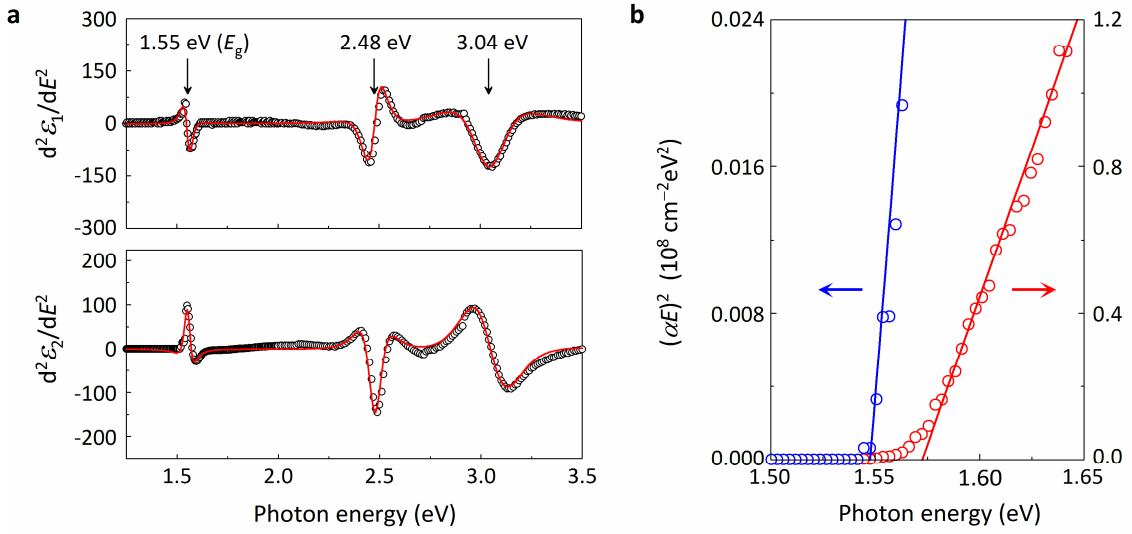


Figure S3 | E_g analysis for α -FAPbI₃. **a**, CP analysis performed for α -FAPbI₃. This analysis was carried out by using a procedure established previously⁵ assuming three transitions in an energy region of $E \leq 3.5$ eV. The open circles denote the experimental data and the solid lines represent the theoretical fitting. The CP energies determined from the analysis are indicated by the arrows. In the CP analysis, the fitting errors were minimized by using different combinations of CP structures. As a result, the transition energies are determined to be 1.55 ± 0.01 eV ($j = -1/2$), 2.48 ± 0.01 eV ($j = -1$) and 3.04 ± 0.01 eV ($j = -1$). Here, $j = -1/2$ and -1 show the one dimensional and excitonic CP transitions, respectively. For the transition at 1.55 eV, the fitting assuming $j = 0$ (two dimensional CP) provides the similar fitting. In addition, for the two transitions at 2.48 and 3.04 eV, similar fitting quality has been obtained assuming the CP transition of $j = -1/2$. The CP energies of 1.55 and 2.48 eV correspond to the E_0 (E_g) and E_2 transitions in Fig. 2b, respectively. **b**, E_g analysis for α -FAPbI₃ using the $(\alpha E)^2$ - E plot. The open circles represent the experimental data and the solid lines show the linear fitting results. The E_g analysis results for two different $(\alpha E)^2$ regions are shown. It can be seen that this analysis gives slightly different E_g values that depend on the analyzed energy region and is less reliable.

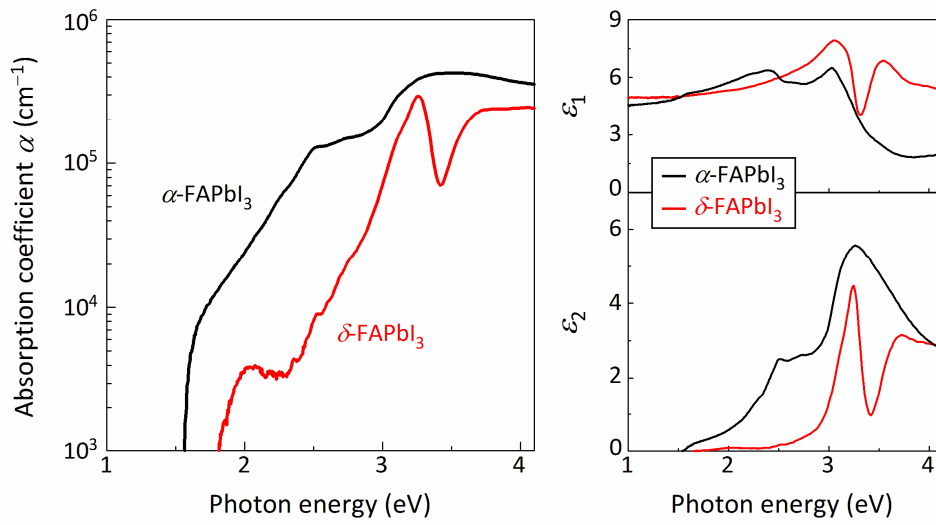


Figure S4 | Optical constants of α -FAPbI₃ and δ -FAPbI₃. α spectra and dielectric functions of the α -FAPbI₃ and δ -FAPbI₃ layers are shown. These spectra were determined based on the self-consistent SE analyses. The optical data of α -FAPbI₃ correspond to those in Fig. 1.

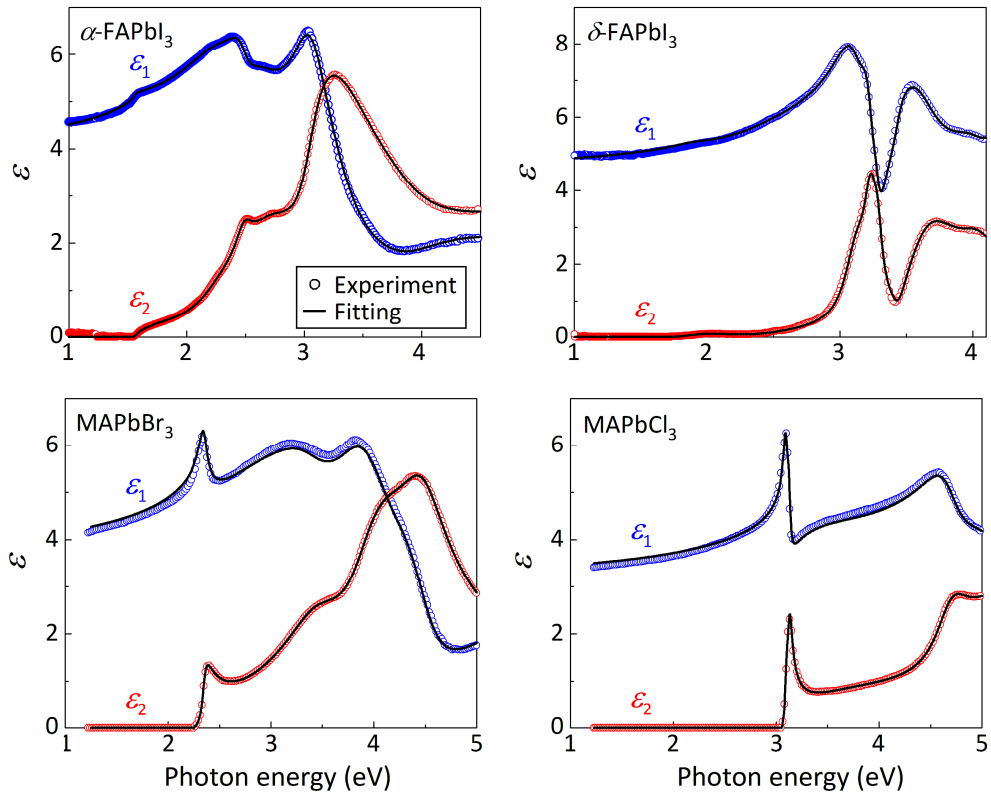


Figure S5 | Dielectric function modeling for hybrid perovskite materials. Dielectric functions of α -FAPbI₃, δ -FAPbI₃, MAPbBr₃ (ref. 9) and MAPbCl₃ (ref. 9) are parameterized assuming several Tauc-Lorentz transitions. The open circles show the experimental dielectric functions shown in Fig. 1b and Fig. S4, and the solid lines indicate the fitting results obtained using the Tauc-Lorentz model. The model parameters are summarized in Table 1.

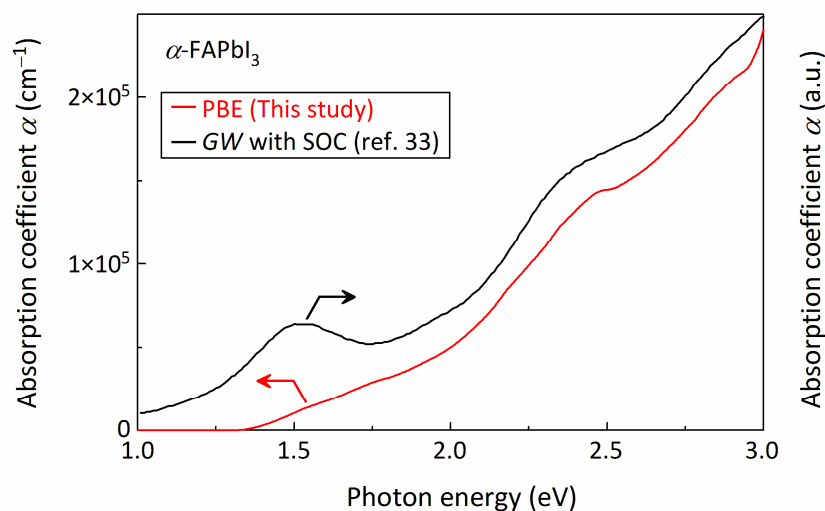


Figure S6 | α spectra of α -FAPbI₃ calculated by DFT. α spectrum of α -FAPbI₃ calculated in this work using PBE is compared with that calculated based on the *GW* method with SOC³³.

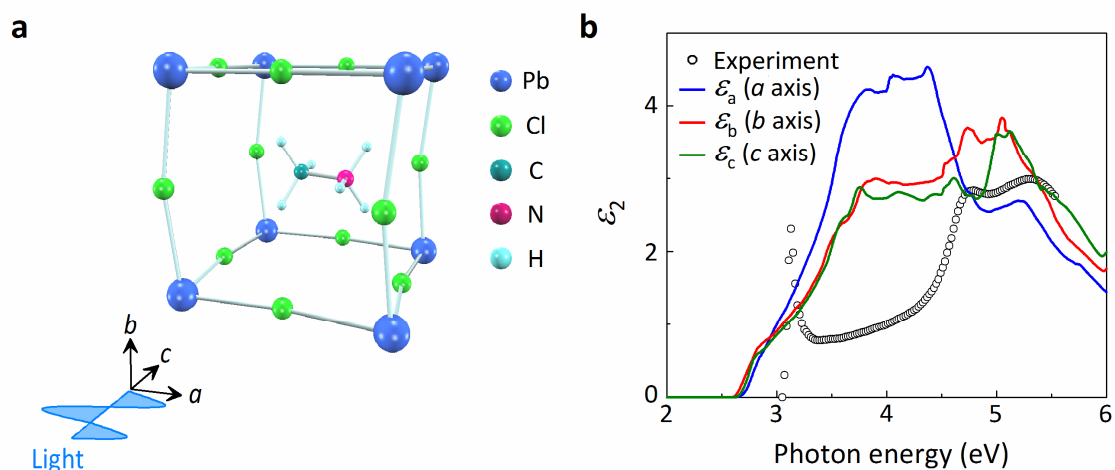


Figure S7 | Dielectric functions of MAPbCl₃ calculated by DFT. **a**, Pseudo-cubic structure of MAPbCl₃ obtained from the DFT calculation. Polarization states parallel to the *a*, *b*, and *c* axes are considered. **b**, ϵ_2 spectra of MAPbCl₃ obtained from experiment (open circles) and DFT calculations (solid lines). For the experimental result, the ϵ_2 spectrum reported in ref. 9 is shown. The ϵ_a , ϵ_b and ϵ_c represent the ϵ_2 spectra calculated assuming the light polarization along the *a*, *b*, and *c* axes in **a**, respectively.

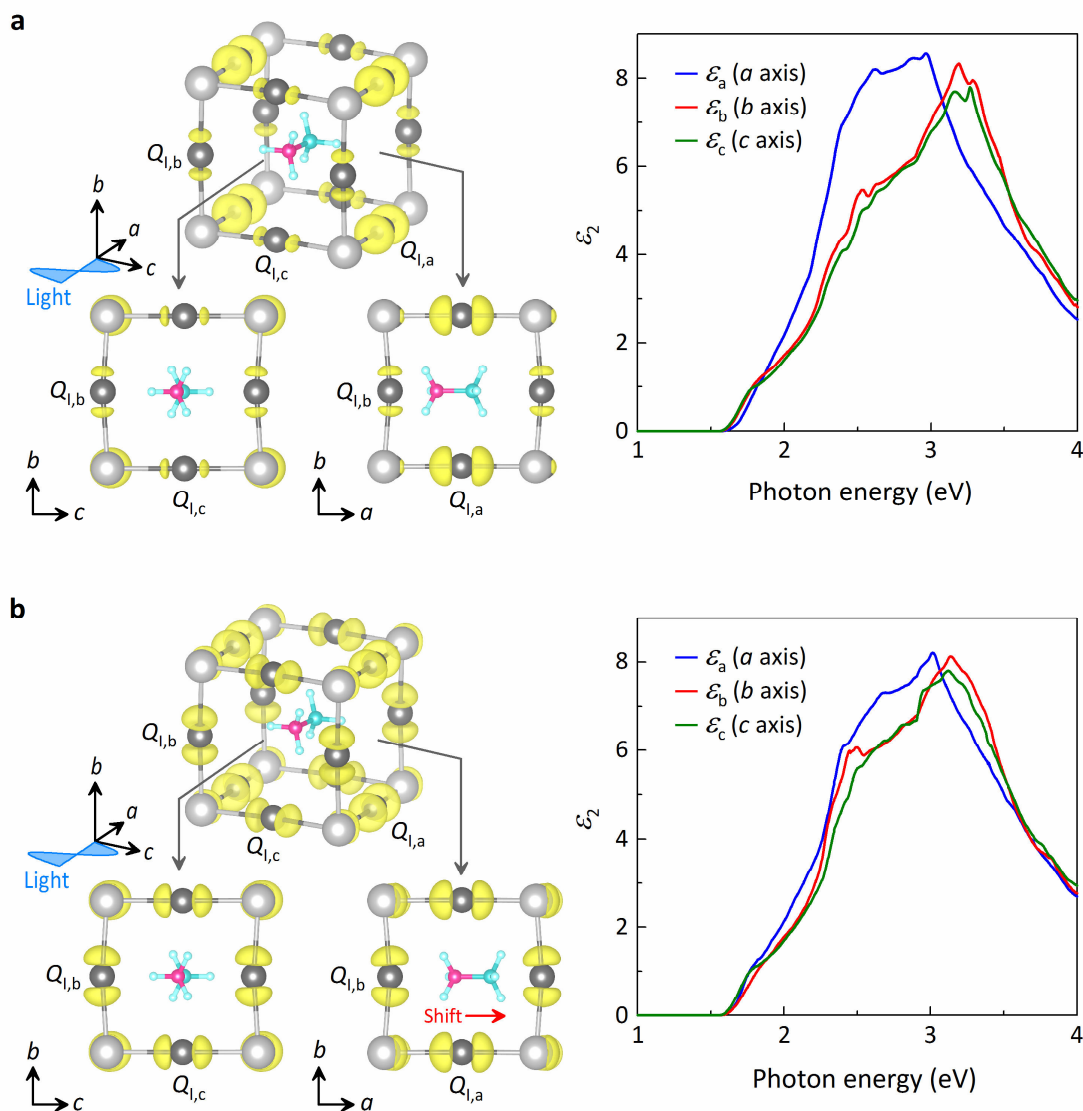


Figure S8 | Effect of the MA⁺ position on the optical transitions in MAPbI₃. **a**, Charge density profiles of the optimized MAPbI₃ structure in the energy region of $E = -0.6 \sim -0.4$ eV from VBM ($E = 0$ eV). These profiles represent the valence charge densities for the E_1 transition at the M_2 point (V_1C_1). The corresponding optical data (ϵ_2 spectra) were adopted from our earlier result⁵. **b**, Charge density profiles of the hypothetical MAPbI₃ structure in the energy region of $E = -0.6 \sim -0.4$ eV from VBM ($E = 0$ eV). In this MAPbI₃, the N atom of MA⁺ is shifted to the center position of the C–N bond in **a**. The charge density profiles represent the valence charge densities for the E_1 transition at the M_2 point (V_1C_1). The dielectric functions calculated from this hypothetical MAPbI₃ structure are also shown. When the N locates away from the I atoms, the distribution of the valence charge density becomes more uniform because of the weaker anti-coupling effect and the strong optical anisotropy disappears.

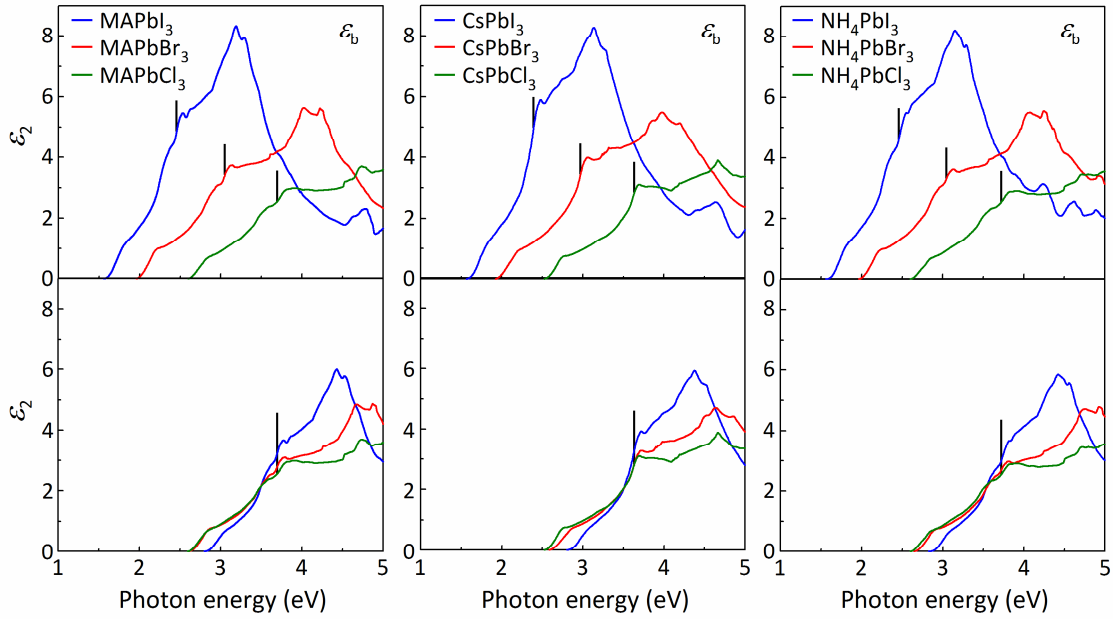


Figure S9 | Dielectric functions of APbX₃ calculated from the DFT and the sum rule. Dielectric functions of MAPbX₃, CsPbX₃ and NH₄PbX₃ (X = I⁻, Br⁻, Cl⁻) calculated in the analysis of Fig. 4b (top panel) and corresponding dielectric functions obtained by applying the sum rule for the APbI₃ and APbBr₃ (bottom panel). The dielectric functions of the top panel have been obtained from the MAPbX₃, CsPbX₃ and NH₄PbX₃ structures determined from the structural optimization of the A-site cation within the fixed PbX₃⁻ cage. In this figure, only the ϵ_2 spectra of the ϵ_b are shown. The bars indicate the energy positions of the E_1 transition at the M_2 point (V_1C_1).

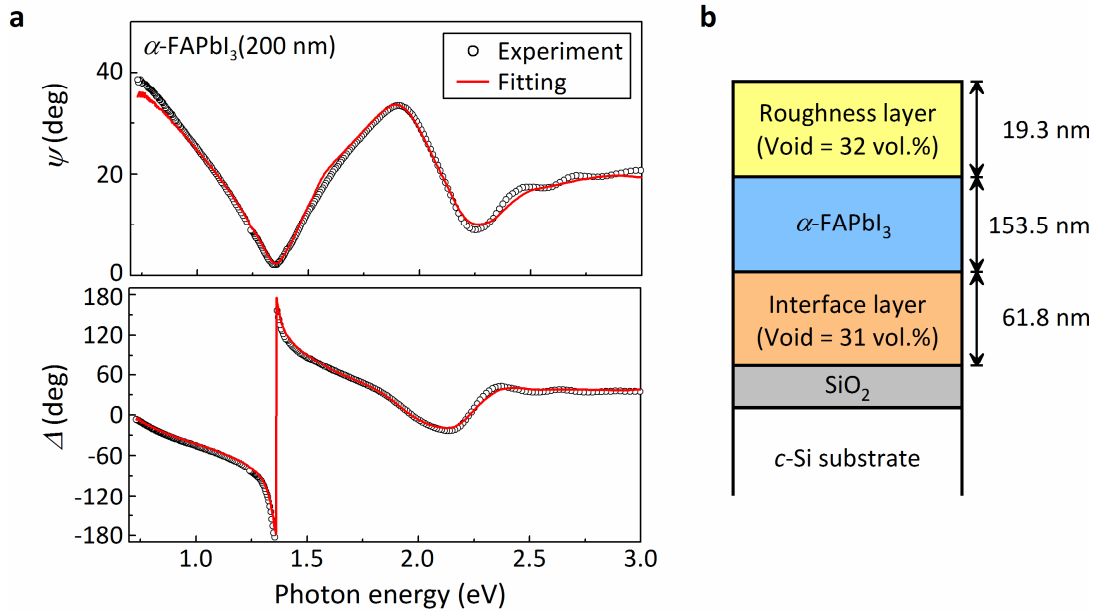


Figure S10 | SE analysis for the α -FAPbI₃ layer. **a**, (ψ , Δ) ellipsometry spectra obtained from the α -FAPbI₃ (200 nm)/SiO₂ (2 nm)/c-Si structure (open circles) and the fitting result calculated using the α -FAPbI₃ dielectric function extracted from the 100-nm-thick layer (solid lines). **b**, Layer structure determined from the SE analysis. The void volume fractions within the surface roughness and the interface layers were employed as free parameters in the fitting analysis and the resulting void volume fractions are shown, together with the thickness of each layer.

Table 1 | Tauc-Lorentz parameters extracted from the dielectric function modeling of Fig. S5. The dielectric function of each material can be calculated as a sum of these Tauc-Lorentz transition peaks. The E_p , A , C , E_g and $\varepsilon_1(\infty)$ denote the peak energy, amplitude parameter, broadening parameter, Tauc gap and constant ε_1 value at high energy, respectively.

Material	Peak	E_p (eV)	A (eV)	C (eV)	E_g (eV)	$\varepsilon_1(\infty)$
α -FAPbI ₃	1	1.557	10.018	0.099	1.543	1.462
	2	1.566	8.849	0.498	1.521	0
	3	2.344	9.041	0.794	1.618	0
	4	2.486	1.028	0.171	1.740	0
	5	2.712	20.435	0.755	2.093	0
	6	3.083	66.516	0.417	2.726	0
	7	3.190	98.353	0.657	2.918	0
	8	3.897	131.316	3.018	3.882	0
δ -FAPbI ₃	1	1.893	1.573	0.404	1.667	2.455
	2	2.291	15.657	1.898	2.288	0
	3	3.127	2.182	0.232	1.690	0
	4	3.232	1.563	0.118	1.803	0
	5	3.285	0.411	0.078	1.695	0
	6	3.439	367.887	0.233	3.411	0
	7	3.611	72.513	0.366	3.398	0
	8	4.021	3.777	0.291	3.305	0
MAPbBr ₃	9	4.638	776.547	0.202	4.388	0
	1	2.258	14.194	0.022	2.245	0.155
	2	2.298	50.951	0.110	2.257	0
	3	2.343	140.251	0.090	2.305	0
	4	2.993	27.511	1.924	2.383	0
	5	3.465	7.641	0.838	2.203	0
	6	3.950	95.354	0.760	3.451	0
	7	4.460	10.132	0.561	3.056	0
MAPbCl ₃	8	8.172	180.269	0.053	5.710	0
	1	3.065	24.330	0.012	3.045	0.076
	2	3.096	177.556	0.046	3.043	0
	3	3.125	219.273	0.052	3.071	0
	4	3.199	34.078	1.516	3.099	0
	5	4.695	10.013	0.397	3.733	0
	6	5.279	17.475	1.421	3.051	0
	7	9.718	209.001	0.053	6.544	0